New Multifunctional Bipyrimidine-Based Chromophores for NLO Active Thin-Film Preparation.

Umut Bora, Stephania Abdallah, Rana Mhanna, Prescillia Nicolas, Ahmet Dok, Yovan de Coene, Stijn Van Cleuvenbergen, Olivier Jeannin, Jean-Pierre Malval, Koen Clays, et al.

10.1002/chem.202302930

RESEARCH ARTICLE

New Multifunctional Bipyrimidine-Based Chromophores for NLO Active Thin-Film Preparation

Umut Bora,[a] Stephania Abdallah,[b] Rana Mhanna,[b] Prescillia Nicolas,[c] Ahmet Dok,[d] Yovan de Coene,[d] Stijn Van Cleuvenbergen,[d] Olivier Jeannin,[c] Jean-Pierre Malval,[b] Koen Clays,[d] Nathalie Bellec,[c] Hale Ocak,[a] Belkiz Bilgin-Eran,[a] Franck Camerel,*[c] and Huriye Akdas-Kiliç*[a,c]

[a] PhD U. Bora, Prof. B. Bilgin-Eran, Prof. H. Ocak, Prof. H. Akdas-Kiliç
Department of Chemistry
Yildiz Technical University
Istanbul, Turkiye
E-mail: hakdas@yildiz.edu.tr
https://avesis.yildiz.edu.tr/hakdas

[b] PhD S. Abdallah, PhD R. Mhanna, Prof. Jean-Pierre Malval
The Mulhouse Materials Science Institute CNRS-UMR 7361
University of Upper Alsace
Mulhouse, France

[c] PhD P. Nicolas, Dr. N. Bellec, Dr. O. Jeannin, Dr. F. Camerel
Univ Rennes, CNRS, ISCR - UMR 6226,
F-35000 Rennes, France
E-mail: franck.camerel@univ-rennes1.fr
https://iscr.univ-rennes.fr/franck-camerel

[d] PhD A. Dok, Dr. Y. de Coene, Prof. S. Van Cleuvenbergen, Prof. K. Clays
Department of Chemistry
Katholieke Universiteit Leuven
Leuven, Belgium

Abstract: New synthesized bipyrimidine-based chromophores presenting alkoxystyryl donor groups carrying aliphatic achiral and chiral chains in the 4 position, connected to electron-accepting 2,2-bipyrimidine cores have been synthesized. Their linear and nonlinear optical properties were investigated as well as their mesomorphic properties by various techniques (light-transmission measurements, polarized-light optical microscopy, differential scanning calorimetry measurements and two-photon excited fluorescence). The derivatives with achiral linear carbon chains were found to exhibit liquid-crystal properties with the formation smectic phases over large temperature ranges which were confirmed by small-angle X-ray scattering analysis via stacking models. The nonlinear optical properties in the solid state for derivatives with C14 and the citronellol chains have been studied by wide-field second-harmonic generation and multi-photon fluorescence imaging, confirming centrosymmetry for these achiral mesogens and their excellent third-order nonlinearity whereas the chiral compound exhibits non-centrosymmetric organization resulting in a strong Second Harmonic Generation at the crystal state.

Introduction

Design of organic molecular compounds for efficient nonlinear optical properties, by judicious engineering, remains a very challenging field of research nowadays.[1] Unlike inorganic crystals widely used in this area,[2] organic compounds structures exhibit unusually large, ultrafast second and third order nonlinear optical properties that are important to the fields of nonlinear optics and in advanced optical device technologies that involve optical signal processing and computing, image reconstruction, data storage, and telecommunication.[3] These important properties have been demonstrated in a large number of structures, phases and states like organic crystals and films,[4] conjugated polymers,[5] monomolecular films[6] and more recently in the field of liquid crystals.[7]

Liquid crystals (LCs), are a special class of compounds which shows multiple phase transitions between crystalline solid and isotropic liquid state. In LCs, molecular order is maintained to a certain extent while the molecule melts. [8] LCs which contain a great combination of order and mobility, are very useful for many scientific and technological applications such as display technologies (LCD, Liquid Crystal Display),[9] electro-optical applications, [13] biological transport systems.[11] Liquid crystals allow by their nature to form well-defined, flexible and anisotropic structures as thin and structured films. In addition, liquid crystalline materials can easily be proceeded from solution, they can be aligned by shear forces or by application of an external field and the active layer can be easily restored thank to their self-healing properties. Very few examples of mesogenic materials with nonlinear optical (NLO) properties are described in the literature and the majority of the work involves only doping of liquid-crystal phases with chromophores. The NLO and mesogenic properties can be controlled by the structural changes on the donor moiety of the molecule.[12] Recently, we demonstrated that pseudo-tetrahedral octupolar compounds presenting donor 3,4-alkoxystyryl groups attached to 2,2'-bipyrimidine give rise to liquid crystal and linear and nonlinear optical properties.[13] In another study, we described similar derivatives involving chiral chains at the 3,4 positions, thermodynamically stable liquid crystal phases presenting strong second harmonic generation (SHG).[14]

In this present contribution, we describe the synthesis and complete physicochemical characterization (including linear and nonlinear optical, mesomorphic, thermal, structural) of a series of octupolar four-branched compounds incorporating a bipyrimidine (BPM) group as an electron-deficient core (Scheme 1) and four divergent vinyl phenyl arms bearing alkoxy aliphatic

10.1002/chem.202302930

RESEARCH ARTICLE

chains on position 4. Initially, we described similar derivatives involving chiral chains at the 3,4 positions, thermodynamically stable liquid crystal phases presenting strong second harmonic generation. Indeed, on each divergent vinyl phenyl arms, one alkoxy aliphatic chain is present on position 4 (aromatic ring) instead of two chains on previously reported. In the liquid crystal field, it is crucial to design the molecular structure in order to get mesogenic properties. Our purpose was to investigate structurally simpler derivatives, study their structure-properties relationship and compare them to our previous studies. Depending on the nature of the alkoxy chain on these arms, the bipyrimidine derivatives exhibit optical properties such as absorption, emission, or NLO behaviours (two-photon absorption and second harmonic generation). Mesogenic properties were observed only for compounds presenting achiral chains whereas the chiral derivative shows no mesophase. Nevertheless, thin-films of this later compound give rise to a clear SHG signal confirming a noncentrosymmetric organisation. We demonstrated that symmetry breaking by judicious functionalization of 3D organic octupoles allows the emergence of multifunctional liquid crystalline or crystalline chromophores which can easily be processed into large, flexible, thin and self-oriented films presenting second harmonic generation responses

Results and Discussion

Synthesis and Characterization. Synthetic pathways previously reported in the literature were used to obtain the new bipyrimidine derivative target compounds.[13] The coupling reaction of commercially available 2-chloro-4,6-dimethylpyrimidine in the presence of nickel chloride, triphenylphosphine and zinc in DMF at 50°C and in an inert atmosphere led to 4,4',6,6'-tetramethyl-2,2'-bipyrimidine compound **1**.[15] To prepare the chiral analogue, the brominated chiral chain, (S)-1-bromo-3,7-dimethyloctane, was prepared by reduction of commercially available (S)-(-)-β-citronellol using Pd/C (10%) catalyst at 5 bar pressure under H_2 atmosphere, followed by bromination with concentrated HBr/H_2SO_4 acid.[16] Aldehyde derivatives **2a-e** were obtained by the Williamson ether synthesis reaction of commercially purchased 4-hydroxybenzaldehyde and the corresponding n-alkyl bromide in DMF in the presence of K_2CO_3 at 150 °C under an inert atmosphere.[17] The targeted products **3a-e** were obtained by Kneovenagel condensation reaction between methyl groups on the bipyrimidine and the corresponding aldehyde in 5M NaOH aqueous solution, catalyzed by aliquat 336 at 70 °C.

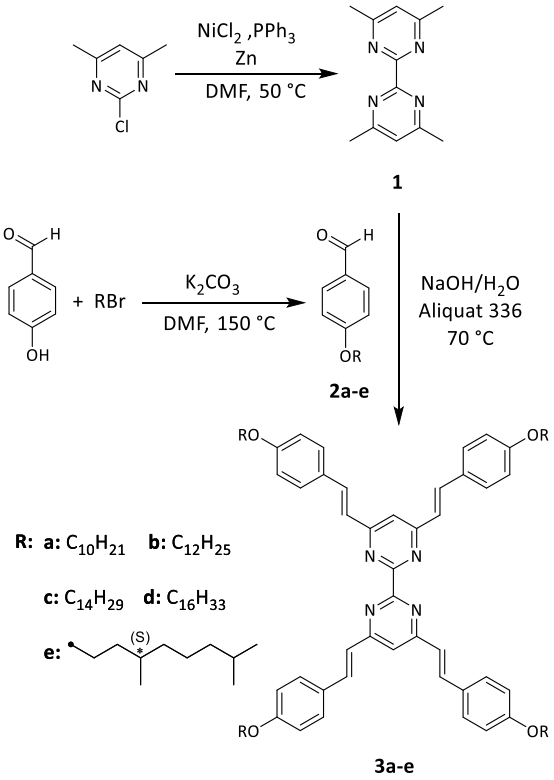

Scheme 1. Synthesis scheme of targeted compounds **3a-e**.

The compounds **3a-e** were obtained in reasonable yields (~30 %) and further fully characterized by NMR, UV-Vis, mass spectroscopy and elemental analysis (See ESI), confirming the expected molecular structure and the symmetrical substitution pattern on the bipyrimidine core.

Linear and Nonlinear Optical Properties in Solution.

Figure 1 shows the one and two-photon photon absorption spectra of the chromophores in THF. The corresponding spectroscopic data are summarized in Table 1. It should be first noted that both the length and the nature of the alkyl chains carried by the alkoxy substituents hardly affect the electronic properties of the octupolar dyes which all exhibit the same photophysical fingerprint. As shown in Figure 1, the one photon absorption (1PA) spectra are all similar with a longest wavelength absorption band located at λ_{MAX} ~ 375 nm and with a significant ε_{MAX} of about ~ 105 000 $M^{-1}cm^{-1}$ (Table 1). A second absorption band is also observed at the blue side of the lowest energy band with a 2.2-fold lower intensity. Such a bands intensity ratio remains invariant irrespective of the alkoxy substituents. As previously observed for similar D-π-A multibranched bipyrimidine-based dyes, [18] these absorption spectra encompass several ππ*-type $S_0 \rightarrow S_n$ transitions implying an electronic delocalisation along the stilbenyl π-conjugated branches with a charge transfer going from the external alkoxy donor groups to the bipyrimidine acceptor core. Interestingly, the two-photon absorption (2PA) spectra of the dyes also exhibit two distinctive 2PA bands (λ_{2PA} ~ 690 nm and ~ 765 nm) which corroborate the occurrence of these $S_0 \rightarrow S_n$ transitions. However, in this case, the 2PA spectra do not match their

10.1002/chem.202302930

RESEARCH ARTICLE

respective 1PA ones. For instance, the 2PA lowest energy band is ~ 2.6-fold less intensive than its higher energy one whose maximum intensity (δ_{MAX}) is in the 250-285 GM range. According to the dipole selection rule relative to the centrosymmetric geometry usually observed for these octupolar series, [19] the $S_0 \rightarrow S_1$ transition is theoretically two-photon forbidden. Such an electronic effect reasonably agrees with the moderate value (~ 90 GM) of the lowest energy 2PA band which should be dominated by the $S_0 \rightarrow S_1$ transition. As shown in Figure 1, all the dyes are fluorescent with an unstructured emissive band in the 380-560 nm range. The dyes display a moderate fluorescence quantum yield with a value of about 0.12. Table 1 gathers all the values of the radiative (k_r) and non-radiative (k_{nr}) rate constants of each relaxed S1 state. One clearly observes that all chromophores present a similar k_r with a mean value of ca. 0.34 x 10^9 s^{-1}. This confirms the electronic equivalency of each emissive state. In addition, the nonradiative relaxation processes, confirmed by Stokes-shift values around 3500 cm^{-1}, clearly constitute the major deactivation channels at the single excited state since k_{nr} are ~ 7-fold higher than k_r. For multibranched octupoles, one very efficient non-radiative pathway responsible for such a severe loss in emissivity should typically stem from an electronic symmetry breaking [28,29] between the Franck–Condon excited state whose electronic configuration implies a full delocalization within the entire multibranched structure and the relaxed emissive state whose excitation is specifically centred on a single D-π-A branch of the dye.

Table 1. Spectroscopic data of the chromophore series in THF

	ε_{abs} /10^3 M^{-1} cm^{-1}	λ_{abs} / nm	λ_{fluo} / nm	E_{00}[a] / eV	Φ_{fluo}	τ_{fluo}[b] / ns	k_r [c] / 10^9 s^{-1}	k_{nr} [c] / 10^9 s^{-1}
3a	105.7	375	432	3.09	0.11	0.33	0.33	2.70
3b	106.6	376	431	3.09	0.12	0.37	0.32	2.38
3c	105.2	375	432	3.09	0.12	0.33	0.36	2.67
3d	107.4	375	430	3.10	0.12	0.33	0.36	2.67
3e	102.5	376	428	3.10	0.12	0.35	0.34	2.51

[a] $E_{00} \approx ½ (\nu_{abs} + \nu_{fluo})$. [b] Average lifetime using a bi-exponential time decay fit. [c] $k_r = \Phi_{fluo}/\tau_{fluo}$, $k_{nr} = (1-\Phi_{fluo})/\tau_{fluo}$.

The luminescence of the compounds in solid state has been recorded by epifluorescence microscopy upon excitation at 365 nm. As shown in fluorescence images of the Figure SI.23 all the chromophores display a light blue emission with the exception of compound **3d** whose luminescence is more greenish. The corresponding fluorescence spectra of dyes are also presented in Figure SI.23 along with the respective excitation spectra which were recorded at their maximum emission wavelengths. For all dyes, the excitation spectrum consists in broad and structured band located in 300-480 nm. Within the series, it can also be observed that the maximum fluorescence wavelength increases with the length of the alkyl chains from λ_{MAX} = 445 nm for **3a** to 493 nm for **3d**.

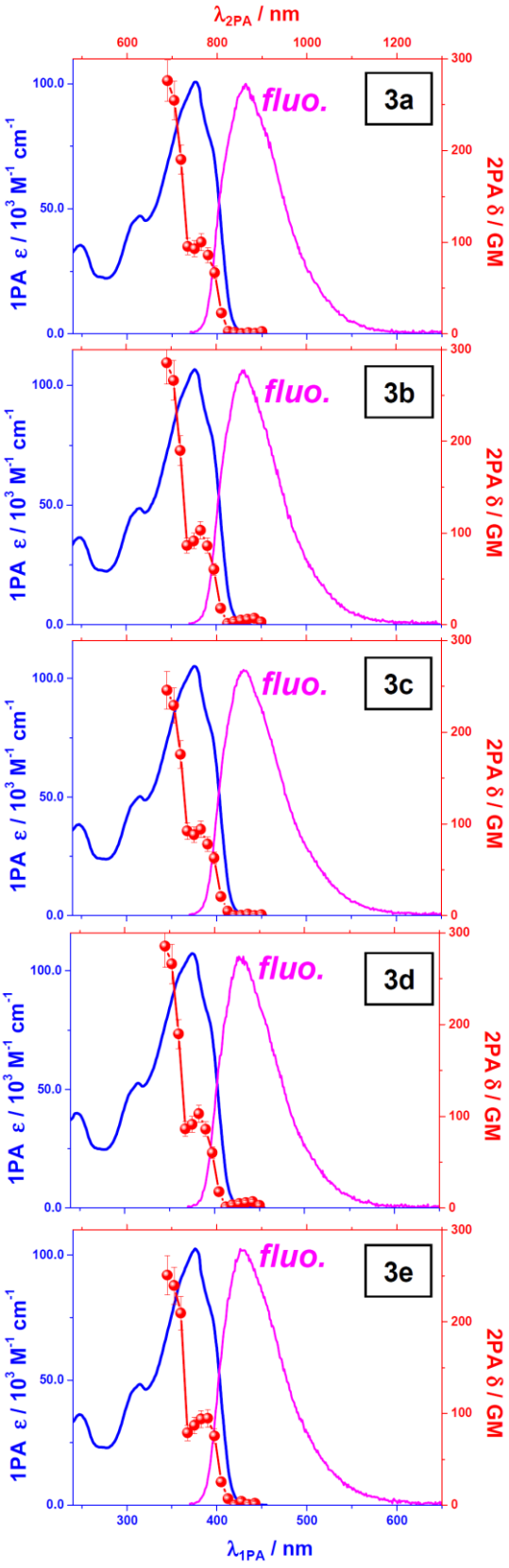

Figure 1. One- (blue lines) and two-photon (red circles) absorption spectra of the compounds **3a-e** in THF. The corresponding fluorescence spectra in THF have been also added.

We employed hyper-Rayleigh scattering to investigate the second-order nonlinear optical properties of the compounds **3c** and **3e** in solution. Measurements were performed in chloroform at 1300 nm, where the multiphoton fluorescence contribution at the second harmonic wavelength was relatively weaker than at other available wavelengths. Through spectral measurement of the second harmonic signal, the remaining multiphoton fluorescence contribution could be accounted for. Hyperpolarizability values were determined by using the internal reference method. Differences in solvent between the compounds and the reference were corrected for by employing local-field correction factors at optical frequencies. We selected compounds **3c** and **3e** for measurement, respectively grafted with achiral and chiral side chains. The hyperpolarizability values, presented in Table 2, are identical within experimental error. From the results for the depolarization ratio (DR), the low value of about 2 clearly reflects the largely octupolar nature of the 4,4',6,6'-tetrasubstituted bipyrimidines. This confirms the earlier observations that the second-order nature of these compounds is mainly determined by the octupolar core, as is also evident from linear and nonlinear absorption and fluorescence measurements.[18] The β_{HRS} values at 1300 nm (in chloroform) are smaller than the ones reported for similar bipyrimidines at 800 nm (in dichloromethane), but this is accounted for by larger resonance enhancement at 800 nm. After correction for this, the $\beta_{HRS,0}$ values are in good agreement with the earlier reported values.[17]

Table 2. Hyperpolarizability Values in Solution

Compound	$\beta_{HRS,1300nm}$ [a]/10 $^{-30}$ esu	$\beta_{HRS,0}$[b]/10^{-30} esu	DR
3c	71±1	43 ± 1	2.2 ± 0.25
3e	94±14	57 ± 8	2.0 ± 0.20

[a] Fluorescence-free values, β (1300 nm), measured by hyper-Rayleigh scattering in CH_3Cl solution (10^{-3} mol L^{-1}). [b] β(0) from the three-level model for octupoles

Thermal Behavior and Self-Organization Properties.

The thermal properties of the various BPM compounds were studied by combining polarized-light optical microscopy (POM) observations and differential scanning calorimetry (DSC) measurements, whereas the molecular organizations in the various phases were analyzed by small-angle X-ray scattering (SAXS) experiments. The thermal behaviors are summarized in Table 3.

The DSC traces of compound **3a** show three exothermic transitions centered at 177, 156 and 116 °C on the cooling curves (ESI Figure SI.16). Above 177 °C, the compound is in an isotropic fluid state. The SAXS patterns recorded in the isotropic state display two broad halos centered at 30.0 and 4.6 Å, corresponding the mean long and short distances between the molecules in the molten state. Upon slow cooling, a characteristic texture of a smectic A mesophase with pseudo fan-shapes and large homeotropic domains readily developed at 177 °C (Figure 2a). Upon further cooling, a new texture appears around 160 °C. This Schlieren-like texture with only four branches defects is characteristic of a smectic C phase (Figure 2b). Around 120 °C, a hardly deformable and uncharacteristic texture, in line with the crystallization of the compound, developed and remains unchanged down to room temperature.

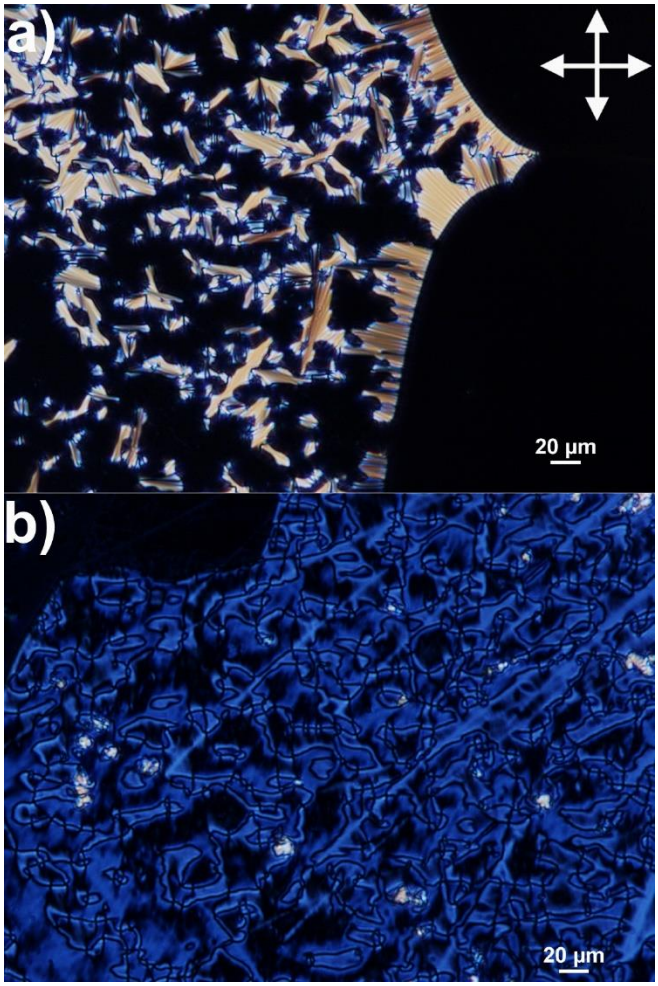

Figure 2. POM images of compound **3a** at 177 °C in the smectic A phase (a) and at 148 °C in the smectic C phase (b).

SAXS patterns recorded upon cooling revealed that the compounds entered in a liquid crystalline state between 180 and 170 °C and crystallized between 150 and 140 °C. The SAXS pattern recorded at 160 °C display only one sharp diffraction peaks in the small angle region at 34.4 Å. This peak is attributed to the lamellar distance in the smectic mesophase. The broad halo observed at 4.5 Å confirmed that the carbon chains are in a molten state and the fluid nature of this organized phase. The SAXS patterns recorded below 140 °C display several sharp peaks over the whole 2θ range explored on the patterns, in line with a crystallization of the compound. The discrepancy observed between SAXS and DSC temperatures is explained by the large difference in heating and cooling rates used between these two techniques.

The DSC recorded upon heating display one exothermic transition centered at 118 °C and two endothermic transitions centered at 157 and 185 °C. The SAXS patterns recorded during heating are all characteristic of the crystalline phases up to 180 °C, at which temperature the compound becomes isotropic. The first two transitions detected on the heating curve are therefore attributed to crystal-to-crystal transformations while the last transition at 185 °C is attributed to isotropization of the

10.1002/chem.202302930

compound. This compound is therefore a monotropic liquid crystalline compound that organizes into a smectic A phase between 177 and 156 °C and a smectic C phase between 156 and 116 °C when cooled at 10 °C/min.

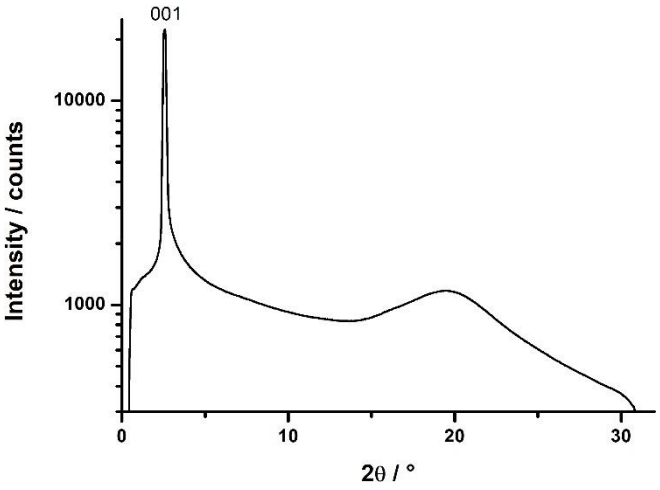

Figure 3. SAXS pattern of compound **3a** recorded at 160 °C upon cooling from the isotropic state (1st cooling).

The first DSC cooling curve of **3b** compound displays a single exothermic transition centered at 172 C°. POM (ESI Figure SI-17) and SAXS analysis confirmed that the compound entered in a LC phase below 172 °C upon cooling from the isotropic phase and remains in a liquid crystalline state down to 30 °C. The SAXS patterns (Figure 4) displays two sharp peaks in the small angle region which can be indexed, in regard to the previous

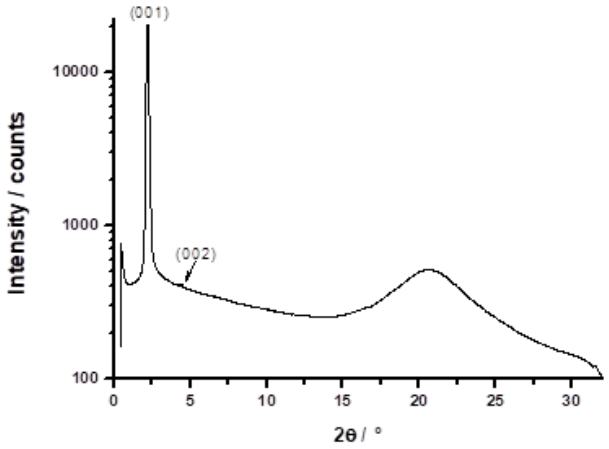

Figure 4. SAXS pattern of compound **3b** at 30 °C.

observations, to the (001) and (002) reflections of a smectic A mesophase. The fluid nature of this organized phase is confirmed by the presence of a broad halo around 4.3 Å. It is interesting to note that this compound remains in the LC state when heated to 120 °C, the temperature above which crystallization of the compound occurs, as evidenced by the appearance of numerous sharp diffraction peaks on all the SAXS patterns. The DSC heating curve finally shows that two close phase transitions occur around 173 °C. The first transition is likely attributed to the melting of the crystalline phase into an LC phase that persists over a very short temperature range (<5°C) before isotropization. This mesophase could not have been properly identified by SAXS.

The DSC traces of compound **3c** display three reversible transitions centered at 116, 143 and 166 °C (ESI Figure SI-18). POM observations confirmed that the compound is in an isotropic state above 166 °C and the SAXS patterns recorded at 170 °C only display two broad halos centered at 34.1 and 4.6 Å (Figure 5). Upon slow cooling from the isotropic state, a characteristic texture of SmA mesophase, with focal conic fans and large homeotropic domains, readily develop below 165 °C. A phase transition is also confirmed by POM around 143 °C with a clear textural change. The temperature dependent SAXS patterns recorded upon cooling confirms the isotropic to mesophase transition between 170 and 160 °C as well as the crystallization of the compound between 110 and 90 °C. The SAXS patterns recorded between 160 and 110 °C display several sharp peaks in the small angle region which can be indexed as the (001), (002) and (003) reflections of a lamellar phase, in line with the smectic phase detected by POM (Figure 6). The SAXS patterns also display a broad halo centered at 4.6 Å, confirming the liquid nature of the phase. However, no change could have been detected by SAXS (Figure 5) around 143 °C and the interlayer distance gradually increase upon cooling. A subtle intralayer reorganization should take place around 143 °C. The same observations can be made upon heating between 117 °C and 167 °C. Based on the previous observations, the phase detected between 143 °C and 94 °C on cooling and between 117 and 144 °C on heating is assigned to a smectic C mesophase. At low temperature, the crystallization is evidenced on the SAXS patterns by the appearance of numerous sharp diffraction peaks over the entire 2θ range explored. However, the crystalline phase formed upon cooling is metastable and a cold crystallization is observed just before the melting point around 90 °C upon heating. This compound is thus organized in a lamellar liquid crystalline state from 165 to 94 °C on cooling and from 117 and 167 °C on heating.

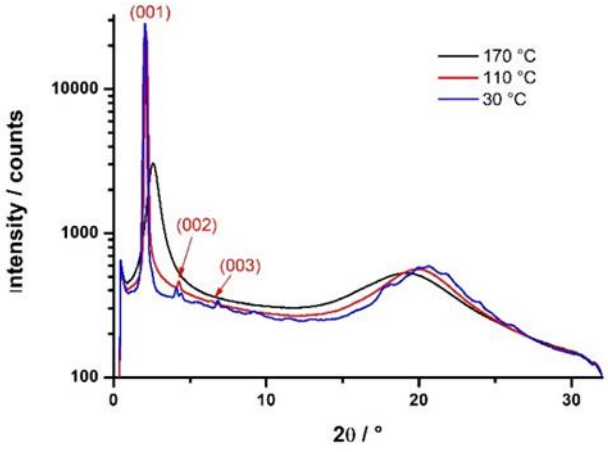

Figure 5. SAXS patterns of compound **3c** recorded at 170, 110 and 30 °C upon cooling from the isotropic state.

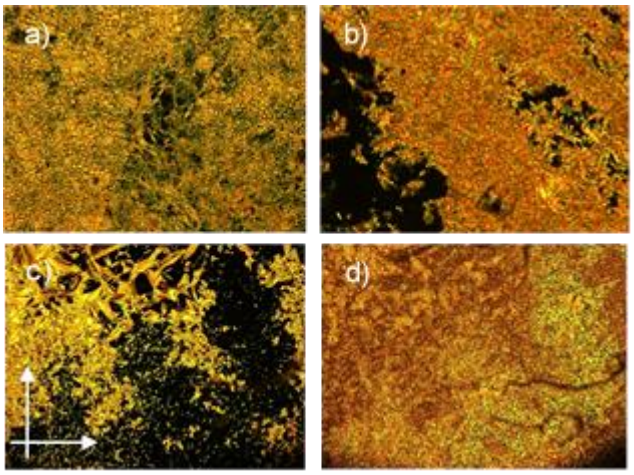

Figure 6. POM images of compound **3d** recorded at a) 149 and b) 135 °C upon cooling. POM images of compound **3c** recorded at c) 162 and d) 127 °C upon cooling.

For compound **3d**, the first cooling DSC cooling curve display three exothermic peaks (ESI Figure SI-19) centered at 160, 141 and 95 °C. Above 160 °C, the compound **3d** is an isotropic state as confirmed by POM observations. The SAXS patterns recorded in this amorphous fluid phase display only two broad halos centered at 35.8 and 4.6 Å, arising from the short and long dimensions of the molecules (Figure 7a).

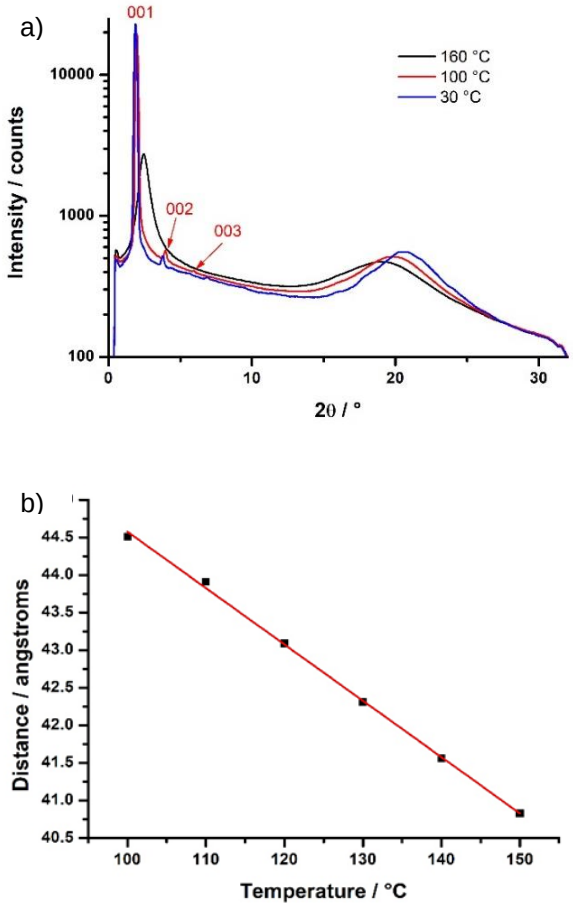

Figure 7. a) SAXS patterns of compound **3d** recorded at 160, 100 and 30 °C upon cooling from the isotropic state; b) Evolution of the lamellar distance in the liquid crystalline temperature range.

Below 160 °C, the compound entered in a liquid crystalline phase and an intense and sharp diffraction peak emerges in the small angle region together with two higher order reflections. These diffraction peaks can be indexed as the (001), (002) and (003) reflections of a lamellar phase. The texture which readily develop under crossed polarizers below 160 °C is characteristic of smectic A phases and supports the SAXS indexation (See ESI). The SAXS patterns also display a broad halo centered at 4.6 Å, characteristic of carbon chains in a molten state and confirms the fluid nature of this organized phase. Despite a clear textural change observed by POM around the endothermic transition at 149 °C (Figure 6), no clear changes could have been detected by SAXS.

The interlamellar distance gradually increase upon cooling in the mesomorphic domain from 160 to 95 °C (Figure 7b). Thus, a subtle organization reorganization should take place in the smectic phase around 141 °C. As already stated, this phase can safely be assigned as a smectic C mesophase. Below 95 °C, the SAXS patterns displays several diffraction peaks in the small angle region and the broad halo around 20 ° in 2θ becomes structured, in line with the crystallization of the compound. Upon further heating, a cold crystallization is observed before the crystal to mesophase transition centered at 126 °C, meaning that the crystalline phase isolated upon cooling is metastable. SAXS analysis confirms that the compound organizes into a lamellar mesophase with an interlayer distance which gradually decrease between 120 and 160 °C.

Table 3. Thermal Behaviour of the 3a-e derivatives

Compound	Transition Temperatures T (°C) [ΔH kJ/mol]
3a	**Heating** → Cr_1 156.9 [8.64] Cr_2 184.7 [28.00] Iso **Cooling** → Iso 177.1 [7.18] SmA 156.1 [0.14] SmC 115.8 [4.71] Cr_1
3b	**Heating** → SmA 116.21 [2.02] Cr 171.36 [5.27] LC 173.38 [3.69] Iso **Cooling** → Iso 172.56 [3.98] SmA
3c	**Heating** → Cr 116.9 [5.82] SmC 144.05 [0.28] SmA 167.0 [3.71] Iso **Cooling** → Iso 165.2 [3.52] SmA 142.0 [0.29] SmC 95.5 [3.19] Cr
3d	**Heating** → Cr 126.15 [21.29] SmC 141.5 [0.77] SmA 161.7 [3.95] Iso **Cooling** → Iso 160.25 [3.80] SmA 140.55 [0.96] SmC 95.40 [5.90] Cr
3e	**Heating** → Cr 161.4 [17.32] Iso **Cooling** → Iso 108.2 [2.33] Cr

[a] Heating and cooling processes were carried out with a "Perkin-Elmer DSC-4000" device at a rate of 10.0°C/minute. Enthalpy values are given in brackets.

Finally, the DSC traces of compound **3e** display one single endothermic peak on the heating curve centered at 161 °C and one single exothermic peak on the cooling curve centered at 108 °C (ESI Figure SI-20). SAXS patterns recorded upon cooling from the isotropic state confirmed that the compound undergoes crystallization between 120 and 110 °C and that this crystalline state melts

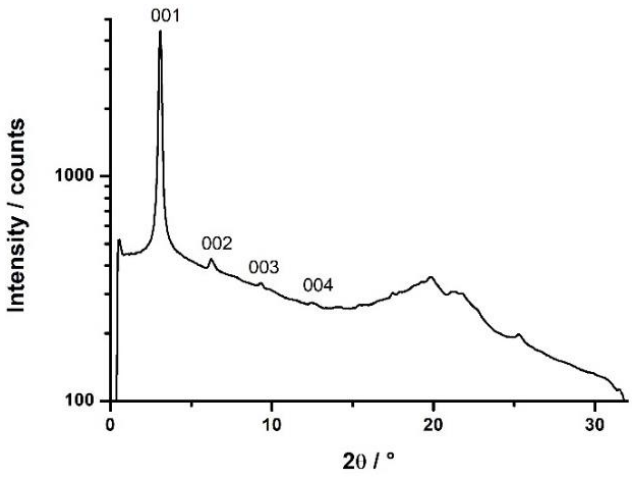

Figure 8. SAXS pattern of compound **3e** recorded at 30 °C.

directly into an isotropic state at 150-160 °C upon further heating, consistent with DSC traces (ESI Figure SI-20). Under crossed polarizers, an uncharacteristic texture, hardly deformable under pressure, readily develops below 120 °C upon cooling from the isotropic state, in line with the crystallization of the compound. This compound is thus deprived of mesomorphic properties. Interestingly, the first diffraction peaks in the small angle region can be indexed as (001) diffraction peaks of a lamellar phase (Figure 8), showing that this compound crystallized into a lamellar phase. This diffraction pattern supports the indexation made for the other compounds.

The mesomorphic investigations clearly demonstrate that the mesomorphic temperature range of each compound occurred in the same range of temperatures whereas mesomorphic properties disappear by using chiral long end-chain group. Additionally, the comparison of the cooling DSC thermograms for compounds **3a-e** concerning the evolution of the phase transition temperatures as a function of the chain length is given in ESI, Figure SI-21. It indicates clearly a decrease of the transition temperatures and a narrowing of the mesomorphic window while the chain's length is increasing.

Solid-State Packing.

Individual molecule can be viewed as two calamitic molecules, with a central rigid and anisotropic bis(styryl)-pyrimidine core carrying two terminal carbon chains, connected by a central C-C bond (Figure 9a). Crystal structures obtained on related bipyrimidine compounds have demonstrated that the two pyrimidine fragments can easily rotate around this central C-C bond with a dihedral angle which can vary between 0 and 70°.[30,31] The planarization of the two calamitic-like pyrimidine fragments can easily explained the formation of smectic A mesophase with the confinement of the rigid parts in disordered sub-layers alternating with sub-layers of molten chains (Figure 9b). The emergence of the smectic C mesophase can probably be ascribed to a slight twist of the two fragments around the central C-C bond.

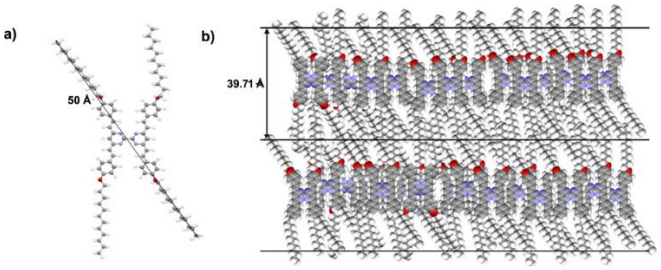

Figure 9. a) Ball and stick representation of compound **3b** in a planar and fully extended configuration; b) Scaled packing model of **3b** molecules in the smectic phase at 30 °C.

Analysis of the (001) peak position as a function of the chain length shows that the interlamellar distance increase linearly from C10 to C16 with the number of carbons on the alkyl chains and this consistent with the presented model in which the aromatic cores are segregated into layers by layers of fully extended carbon chains. The molecular length is longer than the interlamellar distance, indicating that the molten carbon chains are interdigitated. The lamellar distance displayed from **3e** compound is out of the linear regime due to the ramification, the lower temperature measurement and the crystalline nature of the phase.

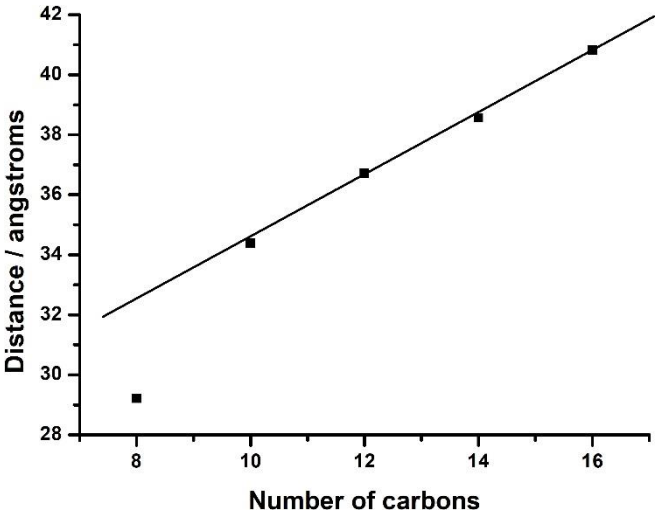

Figure 10. Evolution of the interlamellar distance as a function of the number of carbons on the alkyl chains (**3a** at 160 °C, **3b** at 160 °C, **3c** at 160 °C, **3d** at 150 °C; **3e** (C8(2) chiral chain) at 120 °C).

Nonlinear Optical Properties in the Solid State.

The solid state second-order NLO response was interrogated by wide-field second harmonic generation (SHG) microscopy at a wavelength of 1030 nm for compounds **3c** and **3e**. The samples were prepared in standard liquid crystal cells with a thickness of about 3 micrometers, by heating the sample above the melting point and subsequent slow cooling to room temperature. As can be seen in Figure 11, both samples showed multiphoton fluorescence within the applied voltage gate of the intensifier unit

for a 15 nsec gate width. For the SHG measurements, a relatively weak unstructured response arises for sample **3c**. To account for possible contributions from multiphoton fluorescence (MPF), a spectrum was taken for the same image. In this manner we confirmed that the weak signal arises from MPF rather than SHG. For sample **3e**, a different picture arises. Thin films of the **3e** harmonophore give rise to a clear SHG signal, reflecting the local structure of the film. The origin of the signal was further verified by spectral measurements, confirming the presence of a dominant SHG peak for this sample. In the supporting information we show that the response shows a quadratic dependency on the fundamental power (ESI Figure SI.24), while 3D scanning microscopy demonstrates that the SHG signal stems from the bulk of the polycrystalline domains (Figure SI.25). Unlike MPF, SHG is restricted to noncentrosymmetric structures. In addition to a measurable hyperpolarizability at the molecular level, a macroscopic second-order NLO response requires a noncentrosymmetric (NCS) organization at the supramolecular level. For compound **3e**, the chiral side chains break the centrosymmetric organization characteristic of the achiral **3c** analogue by induction of supramolecular chirality. This result is in line with previous results on similar bipyrimidine chromophores. [17, 18]

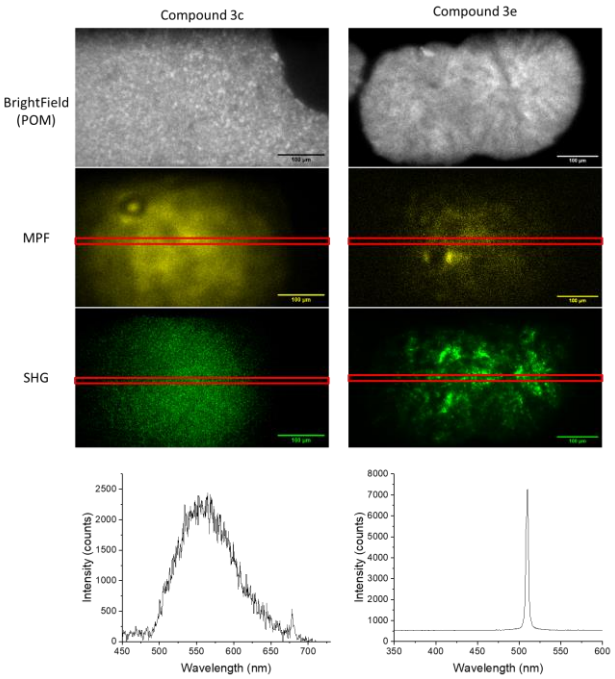

Figure 11. Recorded MPF and SHG images of compound **3c** and **3e** with an incoming S-polarized laser source. Compound **3c** was recorded with a laser beam intensity of 512 mW, while for compound **3e** 60 mW was sufficient. The position of the slit to record the spectra of the images is shown in red (scale bar = 100 µm).

Conclusion

In conclusion, a new series of alkoxy-substituted styryl bipyrimidine cores have been synthesized. Peripheral substitution in the 4-position of the styryl fragments leads to molecular entities strongly emitting around 375 nm with quantum yields around 12% and displaying interesting cubic and quadratic NLO activities at the molecular level in solution in line with previous bipyrimidine derivatives.[17] Compounds **3a-d** were found to be mesomorphic with the formation smectic phases over large temperature ranges confirmed by packing models proposed for compound **3b.** Additionally, the grafting of ramified chiral alkyl chains on 3D octupolar BPM cores, in contrast to compounds with achiral sidechains, didn't give rise to mesomorphic properties nevertheless has allowed again the emergence of NCS crystalline thin-film. SAXS measurements have revealed that this compound **3e** crystallized into a lamellar phase display a marked SHG response under 1030 nm laser irradiation at solid state (determined by SHG measurements). With this work, we demonstrate that 4 chiral 3,7-dimethyloctane sidechains, unlike previously published similar derivatives presenting 4 chiral sidechains, are not sufficient to get liquid crystal properties and we generalize that our simple rational design strategy, i.e. grafting of chiral fragments, allowing the NCS organization of various 3D octupoles into materials processable within thin film layers and has great potential for the development of flexible and large area materials for second-order NLO applications.

Experimental Section

NMR spectra (^{1}H, ^{13}C) were recorded at room temperature on BRUKER Avance III 500 spectrometer, in $CDCl_3$ solution, with tetramethylsilane as external standard.

Microanalysis was performed using a Thermo Fischer Scientific FlashEA 1112 Series elemental analyzer.

Mass spectra were obtained on a Bruker Micro-TOF-Q II instrument and a Q-TOF-LC-MS/MS instrument.

Steady-state absorption and fluorescence spectra. The absorption measurements were carried out with a Perkin Elmer Lambda 2 spectrometer. Steady-state fluorescence spectra were collected from a FluoroMax-4 spectrofluorometer. Emission spectra are spectrally corrected, and fluorescence quantum yields include the correction due to solvent refractive index and were determined relative to quinine bisulfate in 0.05 molar sulfuric acid (Φ_{ref} = 0.52). [22]

Differential scanning calorimetry (**DSC**) was carried out by using NETZSCH DSC 200 F3 instrument equipped with an intracooler. DSC traces were measured at 10 °C/min down to -25 °C.

Optical microscopy investigations were performed on a Nikon H600L polarising microscope equipped with a Linkam "liquid crystal pro system" hotstage. The microscope is also equipped with a UV irradiation source (Hg Lamp, λ = 350-400 nm) and an ocean optic USB 2000+ Uv-Vis-NIR spectrophotometer based on CCD detection technology. This set-up allows the recording of luminescence spectra on solids, liquids, liquid crystalline materials and gels from -196°C up to 420°C between 350 and 1100 nm.

Time-correlated single photon counting. The fluorescence lifetimes were measured using a Nano LED emitting at 372 nm as an excitation source with a nano led controller module, Fluorohub from IBH, operating at 1MHz. The detection was based on an R928P type photomultiplier from Hamamatsu with high sensitivity photon-counting mode. The decays were fitted with the iterative reconvolution method on the basis of the Marquardt/Levenberg algorithm. [23] Such a reconvolution technique allows an overall-time resolution down to 0.15 ns. The quality of the exponential fits was checked using the reduced χ^2 ($\leq$ 1.2).

Two-photon excited fluorescence. The two-photon absorption measurements were performed with femtosecond mode-locked laser pulse using a Ti: Sapphire laser (Coherent, Chameleon Ultra II: pulse duration: ~140 fs; repetition rate: 80 MHz; wavelength range: 680-1080 nm). A relative two-photon excited fluorescence (2PEF) method [24] was employed to measure the two-photon absorption cross-sections, δ. A 10^{-4} M solution of fluorescein[25] in water at pH = 11 was used as the reference (r). The value of δ for a sample (s) is given by the equation 1:

$$\delta_S = \frac{S_S \Phi_r \eta_r c_r}{S_r \Phi_S \eta_S c_S} . \delta_r \qquad (1)$$

where S is the detected two-photon excited fluorescence integral area, c the concentration of the chromophores, and Φ is the fluorescence quantum yield of the chromophores. η is the collection efficiency of the experimental set-up and accounts for the wavelength dependence of the detectors and optics as well as the difference in refractive indices between the solvents in which the reference and sample compounds are dissolved. The measurements were conducted in a regime where the fluorescence signal showed a quadratic dependence on the intensity of the excitation beam, as expected for two-photon induced emission. For the calibration of the two-photon absorption spectra, the two-photon excited fluorescence signal of each compound was recorded at the same excitation wavelength (λ_{exc}: 782 nm) as that used for fluorescein. The laser intensity was in the range of 0.2-2 x 10^9 W/cm^2. The experimental error on the reported cross section is 15 %.

Hyper-Rayleigh scattering: A custom designed optical setup was used to determine the first hyperpolarizabilities of the compounds. The laser (Insight DS+, Spectra-Physics) allows for a tunable output between 680 and 1300 nm. The former delivers femtosecond (~120 fs) pulses at an 80 MHz repetition rate. The output beam ($1/e^2$ < 1.2 mm) has a gaussian profile (M^2 < 1.1) is horizontally polarized (the plane of the optical table). A combination of an achromatic half-wave plate and Glan-Laser polarizer allows to control the output power in accordance to Malus's law. The polarizer is placed in such a way that the extraordinary ray is vertically polarized. The average power which is sent into the sample typically ranges from 500 to 1000 mW. The beam is routed to the input lens (aspheric, f = 8.00 mm) by a series of mirrors. A long pass filter with a cut-off at 690 nm is used to prevent any higher harmonic generation from the laser or the optics from entering the sample. The quartz cuvette (10x4 mm) is placed in a custom translation mount which allows to define the path length of the focal point relative to the side walls. Light is collected at 90° by an achromatic, aspheric condenser lens (f = 30 mm). The collimated beam passes a series of three large broadband dielectric elliptical mirrors to rotate the image 90°. The latter ensures maximal resolution of the spectrograph (vertically oriented slit). The collimated beam is focused on the spectrograph (IS/SM 500, Bruker) with a plano-convex lens, matching the focal length of the spectrograph (f = 200mm, f/8). A blocking edge filter (FF01-720/SP-25, Semrock) ensures high optical density in the laser excitation range. One of two gratings (50 grooves/mm, 600nm blaze or 150 grooves/mm, 500nm blaze) were used, depending on the desired resolution, diffraction range and spectral profile of multiphoton emission spectra. An EMCCD camera (Ixon Ultra 897, Andor Solis) was used to image the spectra.

NLO imaging, the sample was illuminated wide field under normal incidence with femtosecond pulsed infrared (IR) laser light at 1030 nm (Pharos, Light Conversion). The intensity and polarization of the incident IR light is varied by a combination of a zero-order half-wave plate for 1030 nm mounted in a computer-controlled rotation stage (Thorlabs, PRM-Z8) and a Glan-Taylor polarizer selecting for S-polarized light. The sample is irradiated by a long focal length lens (f = 5 cm) which is focused above the sample, so that the incident fundamental light can be considered to a good approximation as a collimated beam and electric field components along the propagation direction (Z) can be neglected. Behind the sample, a 20x objective (Nikon, CFI Plan Fluor 20X CH) collects the light. In the infinity path an IR filter rejects the laser light and a filter wheel selects the transmitted wavelength for SHG (Bandpass, 515 nm, Edmund Optics #65-153), MPF (Longpass, Cut-off wavelength 525 nm, Edmund Optics #84-744) or Brightfield (no filter). A 20 cm tube lens (Mitutoyo) then images the light onto the slit of an imaging spectrometer (Andor, Kymera 328i), coupled to an I-CCD camera (Andor, iStar 340). By switching between a mirror and a grating (150l/mm groove density; blaze = 500 NM), the spectrometer can be used for imaging and spectroscopy respectively. The latter option requires closing the slit of the spectrometer to ensure adequate spectral resolution. For the brightfield imaging, an LED source mounted above the sample was used. This LED source could be polarization selected by a broadband polarizing sheet, positioned perpendicular to a rotatable broadband polarizer in the detection path. In this manner, polarized optical microscopy images could be recorded.

X-ray scattering experiments (**SAXS**) were performed using a XENOCS microsource (50W) with monochromatic Cu Kα radiation (λ = 1.541 Å) and point collimation. The patterns were collected with a Mar345 Image-Plate detector (Marresearch, Norderstedt, Germany). The exposure time at each temperature was 3600 s and the heating or cooling speed between two temperatures was 10 °C/min. The samples were held in Lindeman glass capillaries (1.5 mm diameter). The capillaries were placed inside a Linkam HFX350-Capillary X-Ray stage which allow measurements from -196 °C up to 350 °C with an accuracy of 0.1 °C.

All reagents for synthesis were commercially obtained from Aldrich. The solvents employed for the analysis were spectroscopic grade.

General Procedure For Compounds 3a-e: A stirred mixture of 0.47 mmol 4,4',6,6'-tetramethyl-[2,2']-bipyrimidine (1) and 2.33 mmol the corresponding aldehyde in 15 mL of 5M aqueous sodium hydroxide solution containing 0.10 mmol Aliquat 336 was heated under reflux for 72h. After completion, the mixture was allowed to cool to room temperature, and the precipitate was filtered off, washed with water, diethyl ether and methanol. The crude product was purified by column chromatography (silica gel, eluent CH_2Cl_2/MeOH/Et_3N (100:1:1)), and recrystallized with CH_2Cl_2/MeOH mixture.

4,4',6,6'-Tetrakis((E)-4-(n-decyloxy)styryl)-2,2'-bipyrimidine (**3a**): ($C_{80}H_{110}N_4O_4$; 1191.78 g/mol)
Yield: 0.09 g (32.7%), yellow powder. 1H-NMR (500 MHz, $CDCl_3$): δ (ppm) = δ 7.94 (d, J ≈ 16.1 Hz, 4H, C=CH), 7.60 (d, J ≈ 8.7 Hz, 8H, Ar-H), 7.51 (s, 2H, Ar(N)-H), 7.18 (d, J ≈ 16.1 Hz, 4H, C=CH), 6.94 (d, J ≈ 8.7 Hz, 8H, Ar-H), 4,00 (t, J ≈ 6.6 Hz, 8H, OCH_2), 1.83 – 1.78 (m, 8H, OCH_2CH_2), 1.50 – 1.44 (m, 8H, CH_2), 1.35 – 1.26 (m, 48H, CH_2), 0.88 (t, J ≈ Hz, 12H, CH_3). ^{13}C-NMR (125 MHz, $CDCl_3$): δ (ppm) = 164.31, 163.70, 160.43, 128.66 (Ar-C), 137.08, 129.32, 124.49, 115.03, 113.98 (Ar-CH, C=CH), 68.30 (OCH_2), 32.05, 29.73, 29.71, 29.54, 29.47, 29.37, 26.19, 22.83 (CH_2), 14.27 (CH_3). Anal. Found: C, 80.51; H, 9.84; N, 4.73. $C_{80}H_{110}N_4O_4$ calc.: C, 80.63; H, 9.30; N, 4.70. (Maldi-TOF): m/z 1192.425 ($[M^+H]^+$), $C_{80}H_{110}N_4O_4$ requires 1190.85).

4,4',6,6'-Tetrakis((E)-4-(n-dodecyloxy)styryl)-2,2'-bipyrimidine (**3b**): ($C_{88}H_{126}N_4O_4$; 1304.00 g/mol)
Yield: 0.11 g (36.3%), yellow powder. ^{1}H NMR (500 MHz, $CDCl_3$): δ (ppm) = δ 7.94 (d, J ≈ 16.1 Hz, C=CH), 7.60 (d, J ≈ 8.7 Hz, Ar-H), 7.51 (s, 2H, Ar(N)-H), 7.18 (d, J ≈ 16.1 Hz, 4H, C=CH), 6.94 (d, J ≈ 8.7 Hz, 8H, Ar-H), 4.00 (t, J ≈ 6.6 Hz, 8H, OCH_2), 1.83 – 1.78 (m, 8H, OCH_2CH_2), 1.50 – 1.44 (m, 8H, CH_2), 1.33 – 1.26 (m, 64H, CH_2), 0.88 (t, J ≈ 7.1 Hz, 12H, CH_3). ^{13}C-NMR (125 MHz, $CDCl_3$): δ (ppm) = 164.31, 163.69, 160.43, 128.66 (Ar-C), 137.09, 129.32, 124.48, 115.03, 113.97 (Ar-CH, C=CH), 68.30 (OCH_2), 32.07, 29.81, 29.79, 29.75, 29.73, 29.54, 29.50, 29.37, 26.19, 22.84 (CH_2), 14.27 (CH_3). Anal. Found: C, 80.81; H, 9.91; N, 4.28. $C_{88}H_{126}N_4O_4$ calc.: C, 81.06; H, 9.74; N, 4.28. LC-MS (ESI): m/z 1303.9907 ($[M^+H]^+$), $C_{88}H_{126}N_4O_4$ requires 1302.98).

4,4',6,6'-Tetrakis((E)-4-(n-tetradecyloxy)styryl)-2,2'-bipyrimidine (**3c**): ($C_{96}H_{142}N_4O_4$; 1416.22 g/mol)
Yield: 0.11 g (32.8%), yellow powder. ^{1}H NMR (500 MHz, $CDCl_3$): δ (ppm) = δ 7.94 (d, J ≈ 16.1 Hz, C=CH), 7.60 (d, J ≈ 8.5 Hz, Ar-H), 7.51 (s, 2H, Ar(N)-H), 7.18 (d, J ≈ 16.1 Hz, 4H, C=CH), 6.94 (d, J ≈ 8.5 Hz, 8H, Ar-H), 4.00 (t, J ≈ 6.6 Hz, 8H, OCH_2), 1.83 – 1.78 (m, 8H, OCH_2CH_2), 1.50 – 1.44 (m, 8H, CH_2), 1.38 – 1.27 (m, 80H, CH_2), 0.88 (t, J ≈ 6.8 Hz, 12H, CH_3). ^{13}C-NMR (125 MHz, $CDCl_3$): δ (ppm) = 164.31, 163.70, 160.43, 128.66 (Ar-C), 137.08, 129.32, 124.49, 115.03, 113.97 (Ar-CH, C=CH), 68.30 (OCH_2), 32.08, 29.84, 29.81, 29.75, 29.73, 29.55, 29.51, 29.38, 26.19, 22.84 (CH_2), 14.27 (CH_3). Anal. Found: C, 81.41; H, 10.30; N, 3.96. $C_{96}H_{142}N_4O_4$ calc.: C, 81.42; H, 10.11; N, 3.96. LC-MS (ESI): m/z 1416.1211 ($[M^+H]^+$), $C_{96}H_{142}N_4O_4$ requires 1415.10).

4,4',6,6'-Tetrakis((E)-4-(n-hexadecyloxy)styryl)-2,2'-bipyrimidine (**3d**): ($C_{104}H_{158}N_4O_4$; 1528.43 g/mol)
Yield: 0.08 g (23.4%), yellow powder. ^{1}H NMR (500 MHz, $CDCl_3$): δ (ppm) = δ 7.94 (d, J ≈ 16.1 Hz, 4H, C=CH), 7.60 (d, J ≈ 8.5 Hz, 8H, Ar-H), 7.52 (s, 2H, Ar(N)-H), 7.18 (d, J ≈ 16.1 Hz, C=CH), 6.94 (d, J ≈ 8.5 Hz, 8H, Ar-H), 4.00 (t, J ≈ 6.5 Hz, 8H, OCH_2), 1.83 – 1.78 (m, 8H, OCH_2CH_2), 1.49 – 1.44 (m, 8H, CH_2), 1.36 – 1.19 (m, 96H, CH_2), 0.88 (t, J ≈ 6.8 Hz, 12H, CH_3). ^{13}C-NMR (125 MHz, CDCl3): δ (ppm) = 164.31, 163.70, 160.42, 128.66 (Ar-C), 137.08, 129.32, 124.49, 115.03, 113.97 (Ar-CH, C=CH), 68.30 (OCH_2), 32.07, 29.84, 29.81, 29.76, 29.73, 29.55, 29.51, 29.38, 26.19, 22.84 (CH_2), 14.27 (CH_3). Anal. Found: C, 77.17; H, 10.03; N, 3.45. $C_{104}H_{158}N_4O_4$ calc.: C, 81.73; H, 10.42; N, 3.67. LC-MS (ESI): m/z 1527.1959 ($[M^+H]^+$) $C_{104}H_{158}N_4O_4$ requires 1527.23).

4,4',6,6'-Tetrakis((E)-4-((S)-3,7-dimethyloctyloxy)styryl)-2,2'-bipyrimidine (**3e**): ($C_{80}H_{110}N_4O_4$; 1191.78 g/mol)
Yield: 0.08 g (29.5%), yellow powder. ^{1}H NMR (500 MHz, $CDCl_3$): δ (ppm) = δ 7.94 (d, J ≈ 16.1 Hz, 4H, C=CH), 7.60 (d, J ≈ 8.7 Hz, 8H, Ar-H), 7.52 (s, 2H, Ar(N)-H), 7.18 (d, J = 16.1 Hz, 4H, C=CH), 6.96 (d, J ≈ 8.4 Hz, 8H, 8Ar-H), 4.08 – 4.01 (m, 8H, OCH_2), 1.88 – 1.82, 1.72 – 1.50, 1.38 – 1.13 (3m, 40H, CH, CH_2), 0.96 (d; J ≈ 6.6 Hz; 12H, CH_3), 0,88 (d; J ≈ 6.6 Hz; 24H, CH_3). ^{13}C-NMR (125 MHz, $CDCl_3$): δ (ppm) = 164.31, 163.70, 160.41, 128.66 (Ar-C), 137.07, 129.32, 124.49, 115.04, 113.98 (Ar-CH, C=CH), 66.61 (OCH_2), 39.39, 37.42, 36.29, 24.80 (CH_2), 30.00, 28.12 (CH) 22.86, 22.76, 19.81 (CH_3). Anal. Found: C, 80.32; H, 9.35; N, 4.74. ($C_{80}H_{110}N_4O_4$ calc.: C, 80.63; H, 9.30; N, 4.70. Maldi-TOF: m/z 1192.554 ($[M^+H]^+$ $C_{80}H_{110}N_4O_4$ requires 1190.85).

Acknowledgements

This research has been supported by The Scientific and Technological Research Council of Turkey (TÜBİTAK), in the framework of TÜBİTAK-2232 programme (Project Number 118C273).

Keywords: Bipyrimidine • Chirality • Liquid Crystals • NonlinearOptic • Thin Films

[1] a) S. R. Marder, *J. Mater. Chem.* **2009**, *19*, 7392−7393; b) W. Denk, J. H. Strickler, W. W. Webb, *Science* **1990**, *248*, 73−76.
[2] a) R. Dennington, T. Keith, J. Millam, *in GaussView, Version 5*, Semichem Inc., Shawnee Mission, KS, **2009** b) S. Van Cleuvenbergen, I. Stassen, E. Gobechiya, Y. Zhang, K. Markey, E. Dirk, D. Vos, C. Kirschhock, B. Champagne, T. Verbiest, M.A. van der Veen, *Chem. Mater*. **2016**, *28*, 3203–3209.
[3] M. J. Frisch, G. W. Trucks, H. B. Schlegel, G. E. Scuseria, M. A. Robb, J. R. Cheeseman, G. Scalmani, V. Barone, G. A. Petersson, H. Nakatsuji, X. Li, M. Caricato, A. Marenich, J. Bloino, B. G. Janesko, R. Gomperts, B. Mennucci, H. P. Hratchian, J. V. Ortiz, A. F. Izmaylov, J. L. Sonnenberg, D. Williams-Young, F. Ding, F. Lipparini, F. Egidi, J. Goings, B. Peng, A. Petrone, T. Henderson, D. Ranasinghe, V. G. Zakrzewski, J. Gao, N. Rega, G. Zheng, W. Liang, M. Hada, M. Ehara, K. Toyota, R. Fukuda, J. Hasegawa, M. Ishida, T. Nakajima, Y. Honda, O. Kitao, H. Nakai, T. Vreven, K. Throssell, J. A. Montgomery, Jr., J. E. Peralta, F. Ogliaro, M. Bearpark, J. J. Heyd, E. Brothers, K. N. Kudin, V. N. Staroverov, T. Keith, R. Kobayashi, J. Normand, K. Raghavachari, A. Rendell, J. C. Burant, S. S. Iyengar, J. Tomasi, M. Cossi, J. M. Millam, M. Klene, C. Adamo, R. Cammi, J. W. Ochterski, R. L. Martin, K. Morokuma, O. Farkas, J. B. Foresman, D. J. Fox, *Gaussian 09, Revision A.02*, Gaussian, Inc., Wallingford CT, **2016**.
[4] C. De Bosshard, J. Hulliger, M. Florsheimer, P. Gunter, *Organic Nonlinear Optical Materials* **2001**.
5] G. Koeckelberghs, I. Asselberghs, K. Clays, T. Verbiest, *Proceedings* 8435, Organic Photonics V; 84350D, **2012**.
[6] Tetsuzo Yoshimura, *Molecular Layer Deposition for Tailored Organic Thin-Film Materials* **2023**.
[7] G. Hennrich, A. Omenat, I. Asselberghs, S. Foerier, K. Clays, T. Verbiest, J. L. Serrano, *Angew. Chem., Int. Ed*. **2006**, *45*, 4203−4206.
[8] a) T. J. Sluckin, D. A. Dunmur, H. Stegemeyer, *Crystals that flow: Classic papers from the history of Liquid Crystals*. London: Taylor & Francis, **2004**; b) J.W. Goodby, P.J. Collings, T. Kato, C. Tschierske, H.F. Gleeson, P. Raynes, *Handbook of Liquid Crystals*, Wiley VCH, Weinheim **2014**; c) C. Tschierske, *Angew. Chem. Int. Ed*. **2013**, *52*, 8828–8878.
[9] H. Chen, S.-T. Wu, *Liquid Crystals Today* **2019**, *28(1)*, 4–11.
[10] H. Ocak, B. Karaağaç, H. Akdaş-Kılıç, O. Jeannin, F. Camerel, B. Bilgin Eran, *J. of Mol. Liq.* **2022**, *348*, 118077-118087
[11] L. Nalone, C. Marques, S. Costa, E. B. Souto, P. Severino, *Drug Delivery Trends* **2020**, 141–149.
[12] a) N. Lemaître, A. J. Attias, I. Ledoux, J. Zyss, *Chem. Mater.* **2001**, *13(4),* 1420–1427; b) M. Khalid, R. Hussain, A. Hussain, B. Ali, F. Jaleel, M. Imran, M. A. Assiri, M. U. Khan, S. Ahmed, S. Abid, S. Haq, K. Saleem, S. Majeed, C. J. Tariq, *Molecules* **2019,** *24(11),* 2096.
[13] H. Akdas-Kilig, M. Godfroy, J.-L. Fillaut, B. Donnio, B. Heinrich, P. Kędziora, J.-P. Malval, A. Spangenberg, S. van Cleuvenbergen, K. Clays, F. Camerel, *J. Phys. Chem. C* **2015**, 119(7), 3697–3710.
[14] S. van Cleuvenbergen, P. Kędziora, J.-L. Fillaut, T. Verbiest, K. Clays, H. Akdas-Kilig, F. Camerel, *Angew. Chem. Int. Ed.* **2017**, 56(32), 9546–9550.
[15] J. Nasielski, A. Standaert,,R. Nasielski-Hinkens, *Synth. Commun.* **1991**, *21(7),* 901–906.
[16] D. Ceylan-Erdoğan, E. Ahlatcıoğlu Özerol, H. Ocak, B. Bilgin-Eran, *J. Mater. Sci: Mater. Electron.* **2021**, *32*, 28870–28881.
[17] a) A. Charisiadis, V. Nikolaou, K. Karikis, C. Giatagana, K. Chalepli, K. Ladomenou, S. Biswas, G. D. Sharma, A. G. Coutsolelos, *New J. Chem.* **2016**, *40(7),* 5930–5941 b) A. Brun, G. Etemad-Moghadam, *Synthesis* **2002**,*10*, 1385–1390 c) T. Nakanishi, N. Miyashita, T. Michinobu, Y. Wakayama, T. Tsuruoka, K. Ariga, D. G. Kurth, *J. Am. Chem. Soc.* **2006**, 128(19), 6328–6329 d) T. Asghari, M. Bakavoli, M. Rahimizadeh, H. Eshghi, S. Saberi, A. Karimian, F. Hadizadeh, M. Ghandadi, *Chem. Bio. & amp; Drug Design* **2014**, 85(2), 216–224.
[18] C. Lambert, E. Schmälzlin, K. Meerholz, C. Bräuchle, *Chem. Eur. J.* **1998**, *4*, 512; C. Latouche, H. Akdas-Kilig, J.-P. Malval, J.-L. Fillaut, A. Boucekkine, V. Barone, *Dalton Trans.* **2015**, *44*, 506; P. Savel, H. Akdas-Kilig, J.-P. Malval, A. Spangenberg, T. Roisnel, J.-L. Fillaut, *J. Mater. Chem. C* **2014**, *2*, 295.
[19] a) D. Beljonne, W. Wenseleers, E. Zojer, Z. Shuai, H. Vogel, S. J. K. Pond, J. W. Perry, S. R. Marder, J. L. Brédas, *Adv. Funct. Mater.* **2002**, *12*, 631; b) A. S. Davidov, *Theory of molecular excitons*, Plenum Press, New York, **1971**; c) F. Terenziani, C. Katan, E. Badaeva, S. Tretiak, M. Blanchard-Desce, *Adv. Mater.* **2008**, *20*, 4641.
[20] a) C. Katan, F. Terenziani, O. Mongin, M. H. V. Werts, L. Porrès, T. Pons, J. Mertz, S. Tretiak, M. Blanchard-Desce, *J. Phys. Chem. A* **2005**, *109*, 3024; b) C. Katan, S. Tretiak, M. H. V. Werts, A. J. Bain, R. J. Marsh, N. Leonczek, N. Nicolaou, E. Badaeva, O. Mongin, M. Blanchard-Desce, *J. Phys. Chem. B* **2007**, *111*, 9468.
[21] a) I. Dierking, Textures of Liquid Crystals, Wiley-VCH Verlag GmbH & Co. KGaA, 2003; b) B. Barszcz, A. Bogucki, R.n Świetlik, H. Akdas-Kiliç, F. Camerel, T. Roisnel, Liquid Crystals, 2019, 46, 1403,
[22] R. Meech, D. J. Phillips, *J. Photochem.* **1983**, 23, 193-217.
D. V. Connor, D. Phillips, *Time correlated single photon counting,* Academic Press, London, **1984**.
[23] F. D. Lewis, R. S Kalgutkar, J.-S Yang, *J. Am. Chem. Soc*. **1999**, *121*, 12045-12053.
[24] M. A. Albota, C. Xu, W. W. Webb, *Appl. Opt*. **1998**, *37*, 7352-7356.
[25] C.K. Tung, Y. Sun, W. Lo, S.J. Lin, S.H. Jee, C.Y. Dong, *Microsc. Res. Tech.* **2004**, *65*, 308−314.

10.1002/chem.202302930

RESEARCH ARTICLE

Entry for the Table of Contents

Herein, we described the preparation of bipyrimidine-based chromophores presenting alkoxystyryl donor groups carrying aliphatic achiral and chiral chains on the 4 position. Symmetry breaking by judicious functionalization of 3D organic octupoles allows the emergence of multifunctional liquid crystalline or crystalline chromophores which can easily be processed into large, flexible, thin and self-oriented films presenting second harmonic generation response.

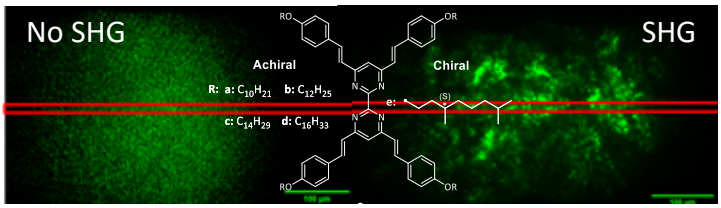

@YildizEdu, @chimie_ISCR, @science@leuven, @UHA68, @AkdasKilic,